Learnable Multi-scale Fourier Interpolation for Sparse View CT Image Reconstruction

Qiaoqiao Ding[1], Hui Ji[1], Hao Gao[2], and Xiaoqun Zhang[3]

[1] Department of Mathematics, National University of Singapore, 119076, Singapore
{matding,matjh}@nus.edu.sg
[2] Department of Radiation Oncology, University of Kansas Medical Center, Kansas City, 66160 KS, USA
hao.gao.2012@gmail.com
[3] Institute of Natural Sciences & School of Mathematical Sciences & MOE-LSC, Shanghai Jiao Tong University, 200240 Shanghai, China
xqzhang@sjtu.edu.cn

Abstract. Image reconstruction in sparse view CT is a challenging ill-posed inverse problem, which aims at reconstructing a high-quality image from few and noisy measurements. As a prominent tool in the recent development of CT reconstruction, deep neural network (DNN) is mostly used as a denoising post-process or a regularization sub-module in some optimization unrolling method. As the problem of CT reconstruction essentially is about how to convert discrete Fourier transform in polar coordinates to its counterpart in Cartesian coordinates, this paper proposed to directly learn an interpolation scheme, modeled by a multi-scale DNN, for predicting 2D Fourier coefficients in Cartesian coordinates from the available ones in polar coordinates. The experiments showed that, in comparison to existing DNN-based solutions, the proposed DNN-based Fourier interpolation method not only provided the state-of-the-art performance, but also is much more computationally efficient.

Keywords: CT Reconstruction · Deep Learning · Fourier Interpolation

1 Introduction

Computed tomography (CT) is one imaging technique widely used in clinical and industry applications. Mathematically, in CT imaging, a projection data (or sinogram) p from a scanning angle $\theta \in [0, \pi)$ at a position $\xi \in \mathbb{R}$ is obtained via the following Radon transform [14]:

$$p_\theta(\xi) = \int_{-\infty}^{\infty} f(\xi \vec{s} + \eta \vec{s}^{\perp}) d\eta, \tag{1}$$

where f is the target image to be reconstructed, $\vec{s} = (\cos\theta, \sin\theta)^\top$ and $\vec{s}^{\perp} = (-\sin\theta, \cos\theta)^\top$. Reconstructing the image f is then about inverting Radon transform from a limited number of observations corrupted by noise. Fourier

slice theorem [2, 21] plays an important role in the inversion of Radon transform, which relates the 1D Fourier transform of projections with the 2D Fourier transform of the image in polar coordinates:

$$F(\omega, \theta) = F(\omega \cos\theta, \omega \sin\theta) = \widehat{p_\theta}(\omega),$$

where F denotes the 2D Fourier transform of the image f, and $\widehat{\cdot}$ denotes 1D Fourier transform. Recall that once $\{F(\omega_x, \omega_y)\}$ in 2D Cartesian coordinates are obtained, the image f can be reconstructed from $\{F(\omega_x, \omega_y)\}$ by inverse DFT. Thus, the CT image reconstruction can then be re-formulated as, given a set of 1D discrete Fourier coefficients $\{\widehat{p_{\theta_k}}(\omega)\}_k$ for a limited number of $\{\theta_k\}_k$ in polar coordinates, how to estimate $\{F(\omega_x, \omega_y)\}$ in 2D Cartesian coordinates.

The interpolation problem in 2D discrete Fourier domain, *i.e.* estimating all 2D Fourier coefficients on Cartesian coordinates from the available measurements on polar coordinates, is indeed a challenging problem. It cannot be simply solved by classic numerical interpolation schemes, *e.g.* linear interpolation. The main reason is that the 2D Fourier coefficients of an image are highly irregular, which contradicts the local smoothness assumption made by classic interpolation schemes. As a result, direct call of classic interpolation schemes will lead to very erroneous results with noticeable artifacts. In the case of sparse view CT where the available measurements are sparse along a limited number of angles, the results can be even worse. Zhang and Froment [22] proposed to tackle such an interpolation problem with a total variation (TV) regularization on the image. While many other regularization techniques introduced in CT reconstruction, *e.g.*, [13, 15, 16, 19, 9, 11, 6], can also be used for regularizing the interpolation in discrete Fourier domain, these regularization strategies are based on some pre-defined image prior, which does not always hold true in practice.

In recent years, DNN-based deep learning has emerged as one powerful tool for CT image reconstruction. By treating the artifacts in the image reconstructed by some method, earlier works used the DNN as a powerful denoiser to remove the artifacts in the result [12, 8, 18, 20]. More recently, the so-called optimization unrolling with DNN-based prior becomes a more preferred approach; see *e.g.* [1, 3, 10, 17, 7, 4, 5]. These methods take some iterative regularization method, and replace the regularization-relating modules by the DNNs with learnable parameters. Note that, in each iteration, these methods needs to perform the projection and back-projection operation, *i.e.* the Radon transform (1) and it adjoint operator. As these operations are computationally expensive, the inclusion of multiple such operations in the network not only makes the computation very time-consuming, but also increases the complexity of network training.

This paper aims at developing a deep learning method for image reconstruction, which not only provide better performance than existing solutions to sparse view CT, but also is much more computationally efficient. The basic idea is to interpret the problem of CT image reconstruction as an interpolation problem in discrete Fourier domain, not as a linear inverse problem in image domain as most methods do. In this paper, we proposed an multi-scale interpolation scheme in discrete Fourier domain with adaptive interpolating weights, which is

predicted by a learnable multi-scale DNN. Note that there is no projection or back-projection is involved in the proposed approach. For performance evaluation, the proposed method is compared with FBP, TV method [15], two deep CT reconstruction methods: LEARN [3] and Learn-PD [1]. The experiments showed that the proposed method outperformed these methods by a noticeable margin, while requiring much less training time.

2 Main body

We first introduced some notations for facilitating the discussion. Let $f(x, y)$, $(x, y) \in \Omega \subset \mathbb{R}^2$ denote the image of spatial attenuation distribution, and $p_\theta(\xi)$ the Radon transform of the object with $\theta \in (0, \pi]$ and $\xi \in [-r, r]$, where r denotes the radius of Ω. For parallel scanning geometry, both $\theta = (\theta_1, \cdots, \theta_L)$ and $\xi = (\xi_1, \cdots, \xi_N)$ are uniformly distributed in the range $[0, \pi) \times [-r, r]$. The 1D Fourier transform of the projection at each view, denoted as $\widehat{q_\theta}$, are distributed on a discrete polar grid in Euclidean space. In other words, the input measurement is $\{F(\omega_k, \theta_\ell)\}$, the 2D Fourier coefficients of the image f on a polar coordinates $\{\omega_k, \theta_l\}_{k,l}$. In order to reconstruct the image f, one needs to estimate the full set of 2D discrete Fourier coefficients of the image f, denoted by $\{F(\omega_{k_1}, \omega_{k_2})\}_{k_1,k_2}$, on Cartesian coordinates, Once we have $\{F(\omega_{k_1}, \omega_{k_2})\}_{k_1,k_2}$, the image can be reconstructed by simply calling an inverse DFT. In short,

$$\{p_{\theta_k}\}_k \to \{F(\omega_k, \theta_l)\}_{k,l} := \{\widehat{p_{\theta_k}}\}_k \to \{F(\omega_{k_1}, \omega_{k_2})\}_{k_1,k_2} \to f := \mathcal{F}^{-1}F,$$

where $\mathcal{F}$ denotes 2D DFT and $\mathcal{F}^{-1}$ denotes its inversion. In the procedure above, the key step is to estimate $\{F(\omega_{k_1}, \omega_{k_2})\}_{k_1,k_2}$ from $\{F(\omega_k, \theta_l)\}_{k,l}$, which is often called the problem of *re-gridding*, an interpolation problem from one grid to a different type of grid. See Fig. 1 for an illustration of the work flow. As the density of measured spectral data decreases rapidly from low to high frequencies, it is a challenging task to interpolate the regions of high frequencies.

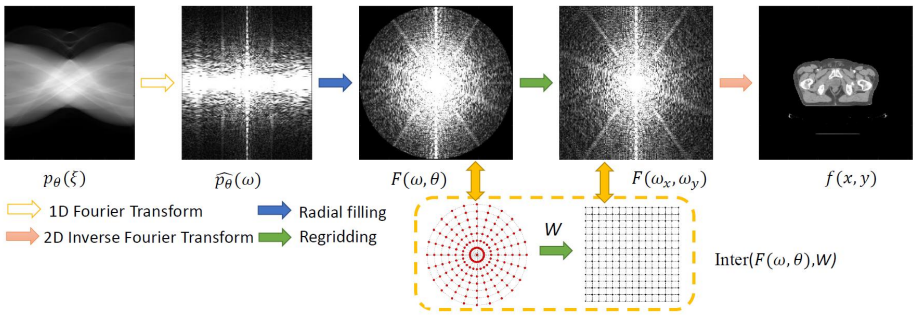

Fig. 1. The work flow of Fourier interpolation (regridding) for image reconstruction

In this paper, we proposed a learnable method for re-gridding in discrete Fourier domain, which excludes the forward/backward projection in the network. The basic idea is to interpolate the missing Fourier coefficient using a weighted summation of its neighbors with adaptive weights. Specifically, for a frequency $(\omega_{k_1}, \omega_{k_2})$ on the Cartesian grid, the missing coefficient is predicted by a weighted average of its K nearest neighbors $\{F(\omega_{k(i)}, \theta_{l(i)})\}_{i=1}^{K}$ on the polar grid:

$$F(\omega_{k_1}, \omega_{k_2}) = \sum_{i=1}^{K} W_{\omega_{k_1},\omega_{k_2}}(i) F(\omega_{k(i)}, \theta_{l(i)}) \tag{2}$$

where $W_{\omega_{k_1},\omega_{k_2}}(i)$ are learnable weights that are adaptive to different frequencies. Such an interpolation scheme is implemented in a multi-scale manner. For low frequencies with dense neighbors in polar coordinates, few neighbors are used for interpolation with smaller K. For high frequencies with sparse neighbors in polar coordinates, more neighbors are used for interpolation with larger K.

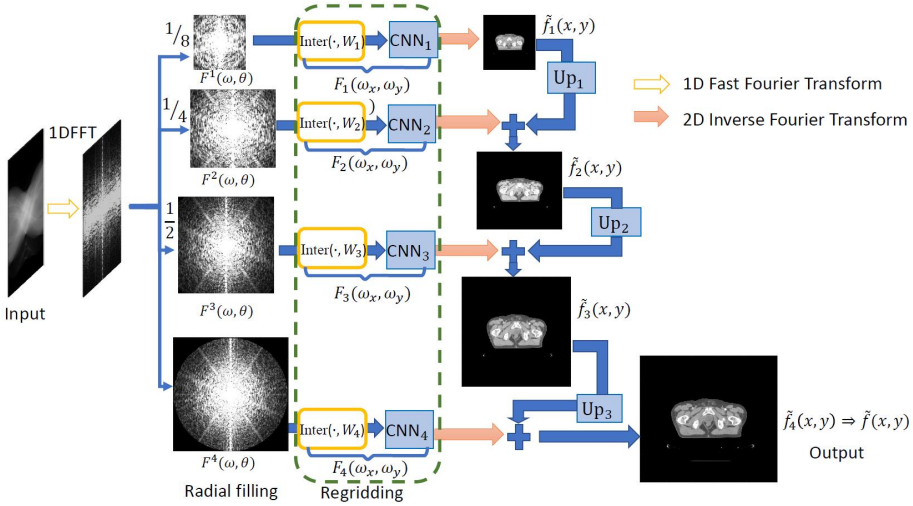

Fig. 2. Diagram of the proposed method.

After the interpolation is done, we have now an initial estimation of all Fourier coefficients on the Cartesian grid. Then, a learnable CNN is introduced to correct possible prediction errors arising in the interpolation. As prediction accuracy decreases from low to high frequencies, we propose a multi-scale CNN-based correction scheme. Briefly, we construct S sets of Fourier coefficients on the polar grid whose range increases from low to high frequencies, denoted by $\{F_s(\omega,\theta)\}_{s=1}^{S}$. Then, after the interpolation and CNN-based correction in discrete Fourier domain, the image can be reconstructed by inverse DFT with respect to different

resolutions. Instead of using such a prediction for estimating the image f at the resolution s, the estimation is done by the concatenation of current estimation and the one from the coarser resolution $s-1$ after up-sampling.

In summary, for each resolution s, the resulting prediction of the image f, denoted by $\tilde{f}_s$, can be expressed as

$$\tilde{f}_s(x,y) = \mathcal{F}^{-1}(\mathrm{CNN}_s(\mathrm{Interp}(F_s(\omega,\theta), W_s), \theta_s)) + \mathrm{Up}_{s-1}(\tilde{f}_{s-1}(x,y), \theta^{up}_{s-1}),$$

where CNN_s denotes the correction network with learnable weights θ_s, Interp denotes the interpolation operator with learnable weight W_s, $F_s(\omega,\theta)$ denotes the input measurement of scale s, $\tilde{f}_s(x,y)$ denotes the output of scale s, and Up_s denotes the upsampling layers from lower to higher resolution image with learnable parameter θ^{up}_s. The image reconstruction $\tilde{f}(x,y)$ is defined as the estimation in the finest resolution $\tilde{f}_S$. In the implementation, we set $S=4$ and $\tilde{f}_0(x,y)=0$. See Fig. 2 for the diagram. Let $\{p^j, f^j\}_{j=1}^J$ denote the training set with J training samples, where each (p^j, f^j) denotes one pair of sinogram and true image. The network is trained by minimizing the following loss function

$$\mathcal{L}(\Theta) = \frac{1}{J}\sum_{j=1}^{J} \|\tilde{f}^j - f^j\|_2^2, \tag{3}$$

where $\Theta := \{\theta_s, W_s, \theta^{up}_s\}$ denotes the whole set of NN parameters.

3 Experiments

To evaluate the performance of the proposed method, we simulated projection data from CT images as follows. The dataset included 6400 prostate CT images of 256×256 pixels per image from 100 anonymized scans, where 80%, and 20% of the data is set for training and testing respectively.

Through the experiments, $K = 2, 4, 6, 8$ are used for the numbers of the nearest neighbors from low to high resolution. For an image of size $N \times N$, the learnable weights, $W_1^{N/8\times N/8\times 2}$,$W_2^{N/4\times N/4\times 4}$, $W_3^{N/2\times N/2\times 6}$,$W_4^{N\times N\times 8}$ at four levels, are initialized with the normalized distance for every point and learned along with the parameters in CNN and Upsampling layers. The standard CNN blocks are stacked with the structure Conv→BN→ReLU. For all the Conv layers in the CNN, the kernel size is set as 3×3, and the channel size is set to 64. The block numbers of CNN are increased over the four levels: starting with 10 blocks for the lowest frequencies and sequentially adding 4 blocks when the resolution level increases. Finally, a CNN with 10 blocks are used in the upsampling stage.

The NN was implemented with PyTorch on a NVIDIA Titan GPU, and trained by the Adam where momentum parameter $\beta = 0.9$, the mini-batch size is 8, and the learning rate is 10^{-4}. The model was trained for 50 epochs. The convolution weights are initialized with constant matrices and the biases are initialized with zeros. Both root mean square error (RMSE) and peak signal to noise ratio (PSNR) are used for quantitative assessment of image quality.

Table 1. Quantitative evaluation of the results (Mean±STD) from different methods.

Angle Number	Noise Level	Method	FBP	TV	FBPConvNet	Learn-PD	LEARN	Proposed
180 views	0%	RMSE	29.35 ± 3.20	25.08 ± 2.81	21.79 ± 2.73	16.21 ± 2.16	$\mathbf{10.79 \pm 1.70}$	13.14 ± 2.34
		PSNR	40.45 ± 0.97	41.35 ± 1.08	43.05 ± 1.04	45.56 ± 0.57	$\mathbf{49.19 \pm 1.29}$	47.50 ± 1.46
	10%	RMSE	36.72 ± 2.98	32.23 ± 2.42	26.91 ± 3.08	28.51 ± 2.39	19.90 ± 1.94	$\mathbf{16.61 \pm 2.57}$
		PSNR	38.48 ± 0.70	39.58 ± 1.05	41.20 ± 0.94	40.65 ± 0.61	43.81 ± 0.82	$\mathbf{45.43 \pm 1.27}$
	20%	RMSE	52.84 ± 4.72	35.64 ± 1.94	23.65 ± 2.53	32.78 ± 1.96	23.76 ± 2.03	$\mathbf{20.86 \pm 2.25}$
		PSNR	35.32 ± 0.75	38.71 ± 0.83	42.32 ± 0.90	39.45 ± 0.52	42.26 ± 0.72	$\mathbf{43.41 \pm 0.91}$
	30%	RMSE	72.05 ± 7.39	39.71 ± 2.07	27.85 ± 2.59	35.92 ± 1.86	34.65 ± 4.70	$\mathbf{22.31 \pm 2.59}$
		PSNR	32.64 ± 0.86	37.77 ± 1.03	40.88 ± 0.79	38.65 ± 0.45	39.03 ± 1.13	$\mathbf{42.83 \pm 1.00}$
45 views	0%	RMSE	82.85 ± 8.55	43.57 ± 2.31	29.95 ± 3.20	36.92 ± 2.62	32.81 ± 2.38	$\mathbf{20.80 \pm 2.57}$
		PSNR	32.42 ± 0.87	36.97 ± 0.86	40.27 ± 0.91	37.96 ± 0.54	39.45 ± 0.62	$\mathbf{43.45 \pm 1.05}$
	10%	RMSE	94.01 ± 7.90	44.87 ± 2.70	33.12 ± 3.34	39.09 ± 3.30	37.16 ± 2.40	$\mathbf{21.05 \pm 2.39}$
		PSNR	30.31 ± 0.71	36.84 ± 0.85	39.39 ± 0.87	37.93 ± 0.72	38.36 ± 0.55	$\mathbf{43.34 \pm 0.98}$
	20%	RMSE	121.28 ± 9.56	48.84 ± 2.23	34.54 ± 3.28	39.06 ± 2.24	39.91 ± 2.15	$\mathbf{25.55 \pm 2.78}$
		PSNR	28.10 ± 0.66	35.97 ± 0.72	39.39 ± 0.81	37.92 ± 0.50	37.86 ± 0.46	$\mathbf{41.65 \pm 0.93}$
	30%	RMSE	156.30 ± 14.11	55.12 ± 3.24	40.25 ± 3.29	48.02 ± 2.26	32.29 ± 2.93	$\mathbf{30.64 \pm 3.32}$
		PSNR	25.90 ± 0.76	34.92 ± 0.69	37.68 ± 0.69	36.13 ± 0.41	39.60 ± 0.79	$\mathbf{40.07 \pm 0.93}$
30 views	0%	RMSE	143.74 ± 11.18	47.21 ± 2.40	42.11 ± 3.91	48.13 ± 2.74	41.85 ± 2.38	$\mathbf{23.11 \pm 2.53}$
		PSNR	26.62 ± 0.68	36.27 ± 0.56	37.30 ± 0.79	36.11 ± 0.49	37.33 ± 0.50	$\mathbf{42.41 \pm 0.91}$
	10%	RMSE	154.24 ± 10.00	48.56 ± 2.41	39.82 ± 4.15	43.77 ± 2.99	45.07 ± 2.27	$\mathbf{26.16 \pm 2.58}$
		PSNR	26.00 ± 0.56	36.02 ± 0.85	37.79 ± 0.86	36.94 ± 0.59	36.68 ± 0.43	$\mathbf{41.43 \pm 0.84}$
	20%	RMSE	181.94 ± 10.17	52.48 ± 2.43	38.37 ± 3.34	53.41 ± 3.31	51.37 ± 2.57	$\mathbf{28.82 \pm 3.10}$
		PSNR	24.56 ± 0.48	35.35 ± 0.54	38.10 ± 0.74	35.21 ± 0.54	35.54 ± 0.43	$\mathbf{40.60 \pm 0.93}$
	30%	RMSE	220.13 ± 14.92	58.44 ± 3.52	43.90 ± 4.96	53.11 ± 3.71	56.23 ± 5.97	$\mathbf{31.82 \pm 3.38}$
		PSNR	22.91 ± 0.57	34.41 ± 0.52	36.94 ± 0.88	35.26 ± 0.61	34.79 ± 0.88	$\mathbf{39.74 \pm 0.90}$

3.1 Parallel Beam CT Reconstruction

In the experiments for parallel beam CT reconstruction, the projection data was down-sampled from 180 to 45 and 30 views to simulate the sparse view geometry. For performance evaluation, the proposed methods is compared to FBP method [2], TV method [15], FBPConvNet [12] and two optimization-unrolling-based deep learning methods: Learn-PD [1] and LEARN [3].

See Table 1 for quantitative comparison of the results from different methods, in terms of RMSE and PSNR. It can be seen that deep learning methods noticeably outperformed two non-learning methods, FBP and TV methods. For the data with 180 views, LEARN is the best performer when measurement is noise-free. In the presence of noise, the proposed method outperformed LEARN, learn-PD and FBPConvNet by a noticeable margin for different noise levels. See Fig. 3 for visual comparison of the results from different methods on one test data with 180 views under different noise levels, and Fig. 4 on the same noise-free test data with different views. Both quantitative and visual comparison showed the advantage of the proposed method over existing solutions to spare view CT reconstruction, especially in the presence of measurement noise.

Computational efficiency is another main motivation of our work. See Table 2 for the comparison of different methods on training/testing time. Owing to the exclusion of the projection/back-projection operators in the proposed method, the proposed method is much more computational efficient than two optimization unrolling methods, LEARN and Learned-PD, in both training and testing. While FBPConvNet is faster than the proposed method, its performance is significantly worse than the proposed one as shown in Table 2.

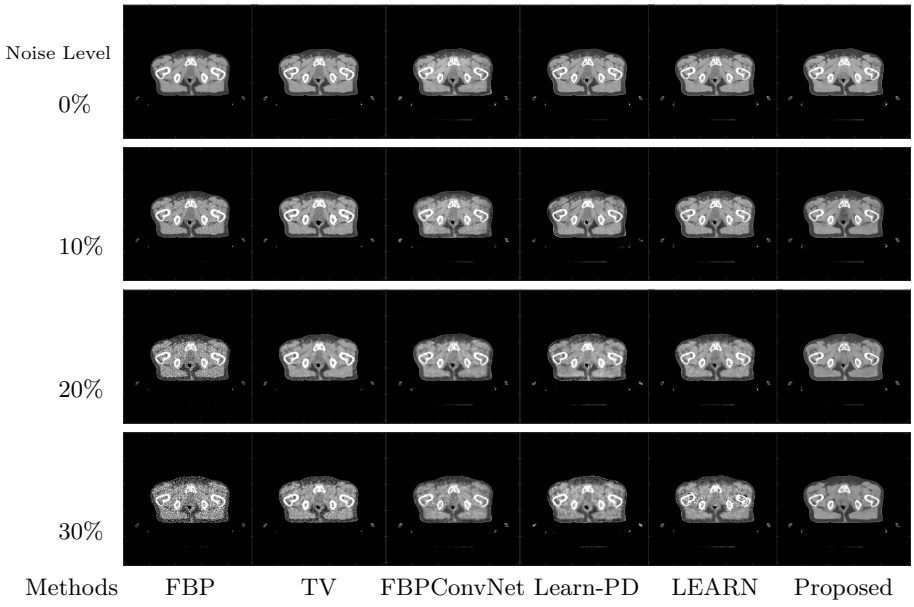

Fig. 3. Parallel beam CT reconstruction with the projection data of 180 views.

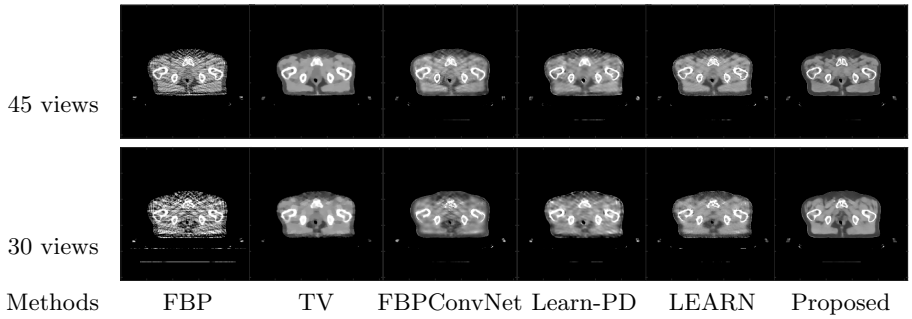

Fig. 4. Parallel beam CT reconstruction with noiseless data: 45 views and 30 views.

Table 2. Comparison of training/testing time of different methods.

		FBP	TV	FBPConvNet	Learn-PD	LEARN	Proposed
Training	180 views	-	-	40 min	6 day	6.2 day	6 hour
	45 views	-	-	40 min	2 day	3 day	5 hour
	30 view	-	-	40 min	1 day	1 day	5 hour
Testing	180 views	0.20 sec	42.67 sec	0.003 sec	2.16 sec	2.27sec	0.05 sec
	45 views	0.04 sec	9.76 sec	0.003 sec	0.55 sec	0.57 sec	0.04 sec
	30 view	0.02 sec	5.76 sec	0.003 sec	0.44 sec	0.39 sec	0.04 sec

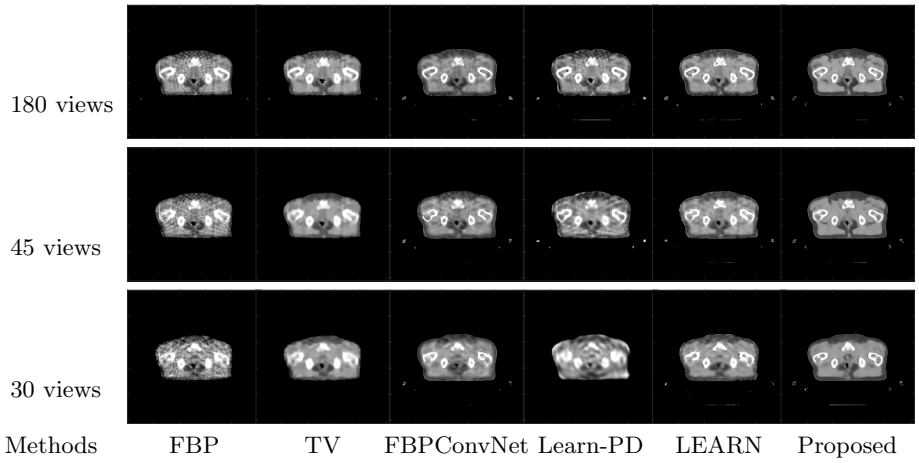

Fig. 5. Fan beam CT reconstruction with noiseless projection data of 45 and 30 views.

3.2 Fan Beam CT Reconstruction

The proposed method is also applied for fan beam CT reconstruction, after re-binning fan beam projection to parallel projection. The experiments are conducted on the noiseless projection data with X-ray source rotated with 180, 45 and 30 views spanned on half circle. See Table 3 for the quantitative comparison of the results from different methods and Figure 5 for visual inspection of the results on sample data. The proposed method remains the top performer, in terms of both quantitative metric and visual quality.

Table 3. Quantitative evaluation of different methods for fan beam CT reconstruction.

		FBP	TV	FBPConvNet	Learn-PD	LEARN	Proposed
180 views	RMSE	85.87±8.88	75.24±2.80	43.14±3.83	50.65±3.04	45.27±2.93	**28.16 ± 3.44**
	PSNR	31.11±0.87	32.25±0.50	37.08±0.76	35.67±0.52	36.65±0.57	**40.91 ± 1.06**
45 views	RMSE	92.81±9.07	78.10±2.13	46.30±5.52	62.54±4.88	53.91±3.04	**33.86 ± 3.97**
	PSNR	30.43±0.83	31.90±0.53	36.49±0.99	33.85±0.68	35.13±0.50	**39.57 ± 1.01**
30 views	RMSE	103.44±8.59	82.34±2.04	52.84±6.24	88.78±10.07	63.36±4.02	**38.95 ± 4.77**
	PSNR	29.48±0.71	31.44±0.51	35.34±0.98	30.83±0.96	33.73±0.55	**38.07 ± 1.06**

3.3 Ablation Study

This ablation study is for evaluating the performance gain brought by three components in sparse view CT reconstruction: (1) CNN-based upsampling vs.

bilinear, (2) multi-scale structure and (3) learnable interpolating weights $\{\boldsymbol{W}_i\}$ vs. fixed weights. The study is conducted on noise-free sample data with 180 views. See Fig. 6 for the comparison of different network architecture with individual component being replaced. It can be seen all three components makes noticeable contributions toward performance gain. In addition, we also evaluate the impact of the values of the hyper-parameter K to the performance. The experiments are conducted on the noisy data of 45 views with 10% noise level. It can be seen from Table 4 that the configuration with $K = 2, 4, 6, 8$ from low to high resolution achieves better performance than other configurations.

Fig. 6. Reconstruction results of different NNs for ablation study.

Table 4. Quantitative evaluations of the results from different configurations on K.

K	2,2,2,2	4,4,4,4	6,6,6,6	8,8,8,8	2,4,6,8
RMSE	26.32±2.81	25.53±3.84	22.88±2.57	21.34±2.49	21.05±2.39
PSNR	41.39±0.94	41.70±1.29	42.61±0.96	43.22±1.00	43.34±0.98

4 Conclusion

This paper presented a multi-scale DNN for sparse view CT image reconstruction, whose key part is to learn an interpolation scheme that converts discrete Fourier transform on polar coordinates to its counterpart on Cartesian coordinates. The proposed method not only provide SOTA performance on CT image reconstruction, but also is very computationally efficient. In future, we would like to extend the proposed method to the case of 3D CT imaging geometry.

Acknowledgment

This work was supported by NSFC (No.11771288 and No.12090024), Shanghai Municipal Science and Technology Major Project (2021SHZDZX0102) and

Singapore MOE Academic Research Fund (MOE2017-T2-2-156 and R-146-000-315-114).

References

1. Adler, J., Öktem, O.: Learned primal-dual reconstruction. IEEE transactions on medical imaging **37**(6), 1322–1332 (2018)
2. Buzug, T.M.: Computed tomography. In: Springer handbook of medical technology, pp. 311–342. Springer (2011)
3. Chen, H., Zhang, Y., Chen, Y., Zhang, J., Zhang, W., Sun, H., Lv, Y., Liao, P., Zhou, J., Wang, G.: LEARN: Learned experts' assessment-based reconstruction network for sparse-data CT. IEEE transactions on medical imaging **37**(6), 1333–1347 (2018)
4. Ding, Q., Chen, G., Zhang, X., Huang, Q., Ji, H., Gao, H.: Low-dose CT with deep learning regularization via proximal forward–backward splitting. Physics in Medicine & Biology **65**(12), 125009 (2020)
5. Ding, Q., Nan, Y., Gao, H., Ji, H.: Deep learning with adaptive hyper-parameters for low-dose ct image reconstruction. IEEE Transactions on Computational Imaging pp. 1–1 (2021). https://doi.org/10.1109/TCI.2021.3093003
6. Dong, B., Shen, Z., et al.: MRA based wavelet frames and applications. IAS Lecture Notes Series, Summer Program on "The Mathematics of Image Processing", Park City Mathematics Institute **19** (2010)
7. Gupta, H., Jin, K.H., Nguyen, H.Q., McCann, M.T., Unser, M.: CNN-based projected gradient descent for consistent CT image reconstruction. IEEE transactions on medical imaging **37**(6), 1440–1453 (2018)
8. Han, Y.S., Yoo, J., Ye, J.C.: Deep residual learning for compressed sensing CT reconstruction via persistent homology analysis. arXiv preprint arXiv:1611.06391 (2016)
9. Hara, A.K., Paden, R.G., Silva, A.C., Kujak, J.L., Lawder, H.J., Pavlicek, W.: Iterative reconstruction technique for reducing body radiation dose at CT: feasibility study. American Journal of Roentgenology **193**(3), 764–771 (2009)
10. He, J., Yang, Y., Wang, Y., Zeng, D., Bian, Z., Zhang, H., Sun, J., Xu, Z., Ma, J.: Optimizing a parameterized plug-and-play ADMM for iterative low-dose CT reconstruction. IEEE transactions on medical imaging **38**(2), 371–382 (2018)
11. Jia, X., Dong, B., Lou, Y., Jiang, S.B.: GPU-based iterative cone-beam CT reconstruction using tight frame regularization. Physics in Medicine & Biology **56**(13), 3787 (2011)
12. Jin, K.H., McCann, M.T., Froustey, E., Unser, M.: Deep convolutional neural network for inverse problems in imaging. IEEE Transactions on Image Processing **26**(9), 4509–4522 (2017)
13. Katsura, M., Matsuda, I., Akahane, M., Sato, J., Akai, H., Yasaka, K., Kunimatsu, A., Ohtomo, K.: Model-based iterative reconstruction technique for radiation dose reduction in chest CT: comparison with the adaptive statistical iterative reconstruction technique. European radiology **22**(8), 1613–1623 (2012)
14. Radon, J.: 1.1 Über die Bestimmung von Funktionen durch ihre Integralwerte längs gewisser Mannigfaltigkeiten. Ber. Verh. Sächs. Akad. Wiss., Math. -Nat. KI. **69**, 262–277 (1917)
15. Sidky, E.Y., Pan, X.: Image reconstruction in circular cone-beam computed tomography by constrained, total-variation minimization. Physics in Medicine & Biology **53**(17), 4777 (2008)

16. Silva, A.C., Lawder, H.J., Hara, A., Kujak, J., Pavlicek, W.: Innovations in CT dose reduction strategy: application of the adaptive statistical iterative reconstruction algorithm. American Journal of Roentgenology **194**(1), 191–199 (2010)
17. Sun, J., Li, H., Xu, Z., et al.: Deep ADMM-Net for compressive sensing MRI. In: Advances in neural information processing systems. pp. 10–18 (2016)
18. Wang, G.: A perspective on deep imaging. IEEE Access **4**, 8914–8924 (2016)
19. Xu, Q., Yu, H., Mou, X., Zhang, L., Hsieh, J., Wang, G.: Low-dose X-ray CT reconstruction via dictionary learning. IEEE transactions on medical imaging **31**(9), 1682–1697 (2012)
20. Ye, J.C., Han, Y., Cha, E.: Deep convolutional framelets: A general deep learning framework for inverse problems. SIAM Journal on Imaging Sciences **11**(2), 991–1048 (2018)
21. Zeng, G.L.: Medical image reconstruction: a conceptual tutorial. Springer (2010)
22. Zhang, X., Froment, J.: Constrained total variation minimization and application in computerized tomography. In: International Workshop on Energy Minimization Methods in Computer Vision and Pattern Recognition. pp. 456–472. Springer (2005)